Supporting Information

Surface wettability engineering of MoS_2 quantum dots-decorated $NiCo_2O_4$ nanospheres for enhanced oxygen evolution reaction

Xu Yue[a,b], *Hongyan Wu,*[a,c] *Yong Zhang*[c] , *Bin Xue*[d]* *and Yuqiao Wang*[a,b,]*

[a]Research Center for Nano Photoelectrochemistry and Devices, School of Chemistry and Chemical Engineering, Southeast University, Nanjing, Jiangsu 211189, China

[b]Yangtze River Delta Carbon Neutrality Strategy Development Institute, Southeast University, Nanjing 210096, China

[c]College of Textile Science and Engineering (International Silk College), Zhejiang Sci-Tech University, Hangzhou 310018, China

[d] Department of Chemistry, College of Food Science and Technology, Shanghai Ocean University, Shanghai 201306, China

E-mail: bxue@shou.edu.cn (B. Xue), yqwang@seu.edu.cn (Y. Wang)

1. Experimental

1.1 Materials

All chemical reagents were of analytical grade and used as received: Sodium molybdate dihydrate ($Na_2MoO_4·2H_2O$), L-Cysteine ($C_3H_7NO_2S$), urea (CH_4N_2O), cobalt(II) nitrate hexahydrate ($Co(NO_3)_2·6H_2O$), nickel(II) nitrate hexahydrate ($Ni(NO_3)_2·6H_2O$), anhydrous ethanol (C_2H_5OH), ethylene glycol ($(CH_2OH)_2$), platinum on carbon (Pt/C, 20 wt%), ruthenium(IV) oxide (RuO_2), and Nafion® perfluorinated resin solution (5 wt%).All materials were procured from Sinopharm Chemical Reagent Co., Ltd. (China). Deionized water (18.2 MΩ·cm) was used throughout the experiments.

1.2 Preparation of MoS_2 Quantum Dots

The MoS_2-QDs were prepared through a hydrothermal route with the following optimized

procedure: Dissolve sodium molybdate dihydrate ($Na_2MoO_4 \cdot 2H_2O$, 0.24 g, 1.0 mmol) and L-cysteine ($C_3H_7NO_2S$, 0.21 g, 1.75 mmol) in 25 mL deionized water under magnetic stirring for 30 min, forming a homogeneous yellow precursor suspension. Transfer the mixture to a 50 mL Teflon-lined stainless steel autoclave and maintain at 200 °C for 10 h under autogenous pressure. Centrifuge the cooled reaction product at 12,000 rpm for 15 min to obtain MoS_2-QDs-1 colloidal solution. For controlled surface functionalization, MoS_2-QDs-(2-4) were synthesized by systematically increasing L-cysteine quantities to 0.24 g (2.0 mmol), 0.27 g (2.25 mmol), 0.30 g (2.5 mmol) and 0.33 g (2.75 mmol), respectively, while keeping other parameters constant. The numerical designation reflects the increasing Mo:S molar ratio from 1:1.75 (MS-QDs-1) to 1:2.75 (MS-QDs-5).

1.3 Preparation of MS@NCO Composite

The prepared procedure was conducted as follows: 25 mL of MoS_2 quantum dot (QD) colloidal suspension was transferred into a 100 mL borosilicate beaker. Subsequently, 0.20 g cobalt(II) acetate tetrahydrate ($Co(CH_3COO)_2 \cdot 4H_2O$), 0.20 g nickel(II) acetate tetrahydrate ($Ni(CH_3COO)_2 \cdot 4H_2O$), and 0.45 g urea ($CH_4N_2O$) were sequentially added to the suspension under continuous magnetic stirring (2000 rpm) until complete dissolution of metal salts was achieved. The homogeneous mixture was then transferred into a 50 mL polytetrafluoroethylene (PTFE)-lined stainless-steel autoclave and subjected to hydrothermal treatment at 120 °C for 4 h in a forced convection oven. The resulting precipitate was collected through centrifugation (8000 rpm, 10 min), repeatedly washed with deionized water and absolute ethanol (3 cycles each), then vacuum-dried at 60 °C for 12 h. For subsequent thermal processing, 0.5 g of the intermediate product was uniformly dispersed in a porcelain combustion boat and annealed in a tube furnace under ambient atmosphere. The thermal protocol involved ramping to 350 °C at 5 °C min^{-1} heating rate, maintaining isothermal conditions for 2 h, followed by natural cooling to room temperature to yield the final MS@NCO composite.

1.4 Electrocatalyst Preparation

The catalyst ink was formulated by homogenizing 2.0 mg active material with 0.5 mg acetylene black conductive additive and 50 μL Nafion binder (5 wt%) in 2.0 mL mixed solvent (1:1 v/v ethanol/water) through 30-minute ultrasonication (40 kHz bath). A precisely controlled 20 μL aliquot was drop-cast onto the GC substrate, yielding a loading of 0.42 mg cm^{-2}, followed by ambient drying.

1.5 Characterization

The microstructural and compositional analysis was performed using advanced characterization techniques: morphological evaluation via field emission scanning electron microscopy (FE-SEM, FEI Inspect F50, 20 kV) with energy-dispersive X-ray spectroscopy (EDS) for elemental mapping, nanostructural investigation through high-resolution transmission electron microscopy (HR-TEM, Thermo Scientific Talos F200X, 200 kV) equipped with selected-area electron diffraction (SAED), crystallographic analysis by X-ray diffraction (XRD, Shimadzu XRD-6100 LabX, Cu Kα λ=1.5406 Å, 2θ=10°-80°), surface chemistry profiling using X-ray photoelectron spectroscopy (XPS, Thermo Scientific K-Alpha+, Al Kα 1486.6 eV) with charge compensation, molecular bonding analysis via Fourier-transform infrared spectroscopy (FT-IR, Thermo Scientific Nicolet iS50, ATR mode, 400-4000 cm^{-1}), and surface wettability assessment through dynamic contact angle measurements (LAUDA Scientific LSA100, 5 μL H_2O sessile drop).

1.6 Electrochemical Evaluation

All electrochemical measurements were conducted using a CHI 760E electrochemical workstation in 1.0 M KOH electrolyte (pH 13.6). A standard three-electrode configuration was employed: Catalyst-modified glassy carbon (GC, 3 mm diameter) as a working electrode, graphite rod as a counter electrode, and saturated calomel electrode (SCE) as a reference electrode.

The potential conversion formula relative to the standard hydrogen electrode (RHE) is as follows:

$$E_{RHE} = E_{SCE} + 0.059 \times pH + 0.241$$

where E_{RHE} and E_{SCE} are potential vs. standard hydrogen electrode and potential vs. saturated calomel electrode.

The OER activity was evaluated through linear sweep voltammetry (LSV) at 2 mV s^{-1} scan rate with 90% iR-compensation based on solution resistance derived from electrochemical impedance spectroscopy (EIS) measurements.

Kinetic analysis was conducted through EIS in the 0.01-100 kHz frequency range combined with variable-scan-rate cyclic voltammetry (20-140 mV s^{-1}) for double-layer capacitance (C_{dl})

determination.

The electrochemical active surface area (*ECSA*) is calculated as following equation[1]:

$$ECSA = \frac{C_{dl}}{C_s}$$

where C_s is general specific capacitance of smooth electrode (0.04 mF cm^{-2}).

Catalyst stability was assessed via chronopotentiometric testing under constant current density (400 mA cm^{-2}) with continuous operational monitoring spanning 24 hours (25℃).

2. Computational Fluid Dynamics Modeling

Numerical simulations were implemented in COMSOL Multiphysics® v6.0 (Burlington, MA) to investigate oxygen bubble detachment dynamics at catalyst-electrolyte interfaces. The Multiphysics framework incorporated five essential modules:

2.1 Multiphase Geometric Construction

The 2D axisymmetric multiphase model comprised: (i) a catalyst solid phase with experimentally determined contact angles ($\theta = 92°$), (ii) a vertically aligned liquid electrolyte column (H = 20 mm) governed by gravitational effects, and (iii) an oxygen gas phase nucleus (r_0 = 1 mm), with interfacial dynamics resolved through surface-adaptive coordinate transformation techniques.

2.2 Material Property Assignment

Physicochemical parameters were defined based on experimental conditions as followings.

Parameters	Value	Source
Electrolyte viscosity	1.0 mPa·s	1.0 mol L^{-1} KOH at 25°C
Oxygen viscosity	20.3 μPa·s	NIST REFPROP database
Surface tension	72 mN/m	Water-air interface

Parameters	Value	Source
Contact angle	θ = 92°	Experimental measurements

2.3 Governing Equations System

The phase-field method solved the coupled Cahn-Hilliard and Navier-Stokes equations:

The Cahn–Hilliard equation is written as[2]:

$$\frac{\partial c}{\partial t} = D\nabla^2(c^3 - c - \gamma\nabla^2 c)$$

where D is a diffusion coefficient with units of Length^2/Time and $\sqrt{\gamma}$ gives the length of the transition regions between the domains. Additionally, the quantity $\mu = c^3 - c - \gamma\nabla^2 c$ is identified as a chemical potential.

The incompressibility Navier-Stokes equation is written as[3]:

$$\frac{Du}{Dt} = \frac{\partial u}{\partial t} + (u \cdot \nabla)u = v\nabla^2 u - \frac{1}{\rho}\nabla p + \frac{1}{\rho}f$$

where $v = \mu/\rho$ (kinematic viscosity), **u** is the flow velocity, ρ is the (mass) density, p is the pressure, and **f** is the external source.

The phase field model is used to track the evolution of gas-liquid-solid interface[4]:

$$\frac{\partial \varphi}{\partial t} + u \cdot \nabla\varphi = \nabla \cdot \frac{\gamma\lambda}{\varepsilon_{pf}^2}\nabla\psi$$

$$\psi = -\nabla \cdot \varepsilon_{pf}^2\nabla\varphi + (\varphi^2 - 1)\varphi + \frac{\varepsilon_{pf}^2 \partial f}{\lambda\ \partial\varphi}$$

where $\varphi = phipf$, $\lambda = \frac{3\varepsilon_{pf}^2\sigma}{\sqrt{8}}$, and $\gamma = \chi\varepsilon_{pf}^2$.

2.4 Boundary Condition Specification

The multiphysics boundary configuration encompassed: (i) no-slip velocity boundary with dynamic contact angle implementation ($\theta = 92°$) at catalyst interfaces, (ii) atmospheric pressure outlet (p = 101.325 kPa) at upper domain boundaries, (iii) axisymmetric flux continuity along central rotation axis, and (iv) quiescent initialization [$u(r,z,t_0) = 0$; $p(r,z,t_0) = \rho g h(r)$] reflecting hydrostatic equilibrium.

2.5 Adaptive Mesh Refinement

The adaptive mesh refinement strategy employed a hybrid discretization scheme comprising: (i) 5-layer inflation boundary mesh (growth rate 1.2 %) adjacent to catalytic surfaces, (ii) interface-conforming triangular elements (h_{min} = 0.02 μm) resolving gas-liquid menisci, and (iii) background quadrilateral elements (h_{max} = 2 μm) in bulk domains, with grid convergence index (GCI) < 3% achieved through successive h-refinement cycles.

2.6 Density functional theory calculation

Spin-polarized density functional theory calculations were conducted using the Vienna Ab initio Simulation Package (VASP) employing the Perdew-Burke-Ernzerhof (PBE) generalized gradient approximation (GGA) for exchange-correlation interactions. Structural optimizations proceeded via conjugate gradient minimization until reaching convergence thresholds of 10^{-4} eV for total energy and 0.05 eV·Å^{-1} for residual atomic forces. The heterostructure model incorporated a periodic slab geometry with a 15 Å vacuum spacer along the z-axis to avoid periodic interactions. Initial crystallographic configurations for $NiCo_2O_4$ and MoS_2 were obtained from the Materials Project Database (materialsproject.org). The computational model was conducted with a MoS_2 quantum dots anchored on the thermodynamically stable $NiCo_2O_4$(200) surface.

Supplementary Figures

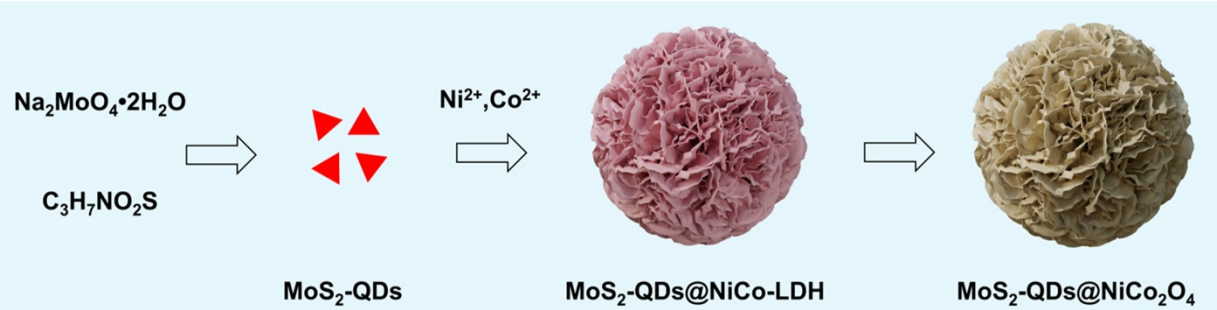

Fig. S1 Schematic illustration of the hydrothermal synthesis process for MS@NCO.

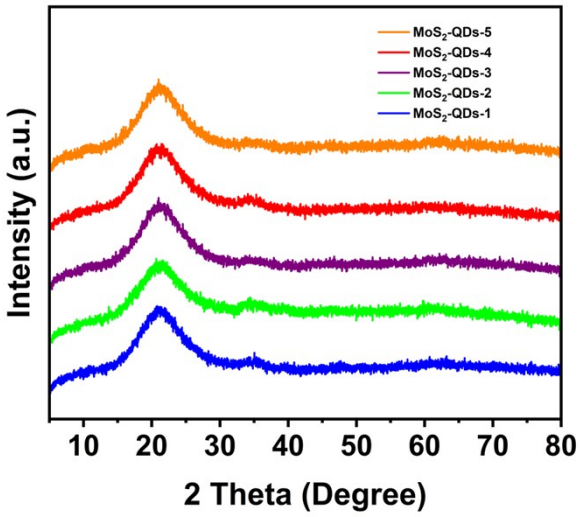

Fig. S2 XRD pattern of the synthesized MoS_2-QDs.

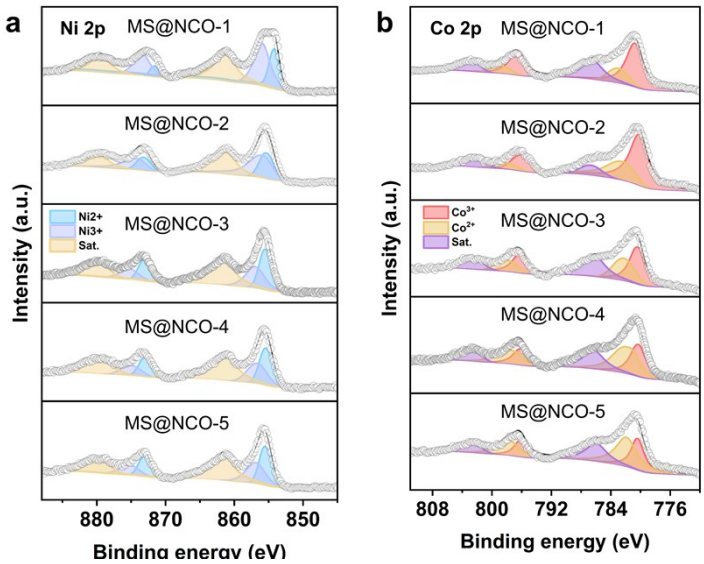

Fig. S3 XPS spectra of (a) Ni 2p and (b) Co 2p in MS@NCO.

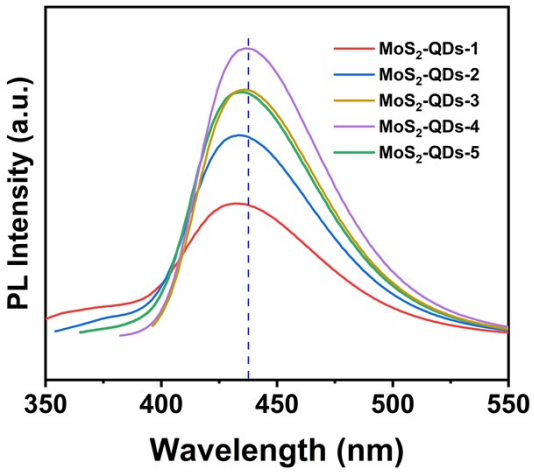

Fig. S4 Fluorescence excitation spectra of MoS_2-QDs series.

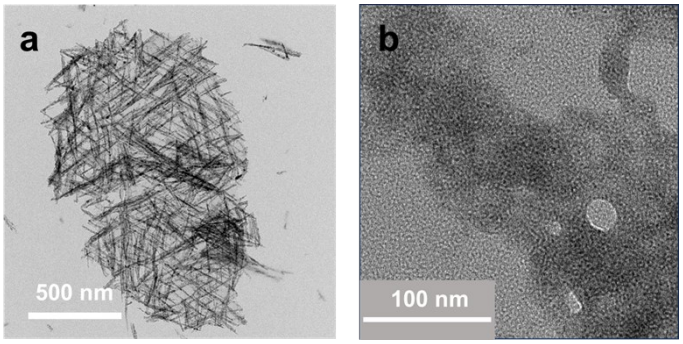

Fig. S5 TEM images of (a) pristine $NiCo_2O_4$ and (b) MoS_2-QDs.

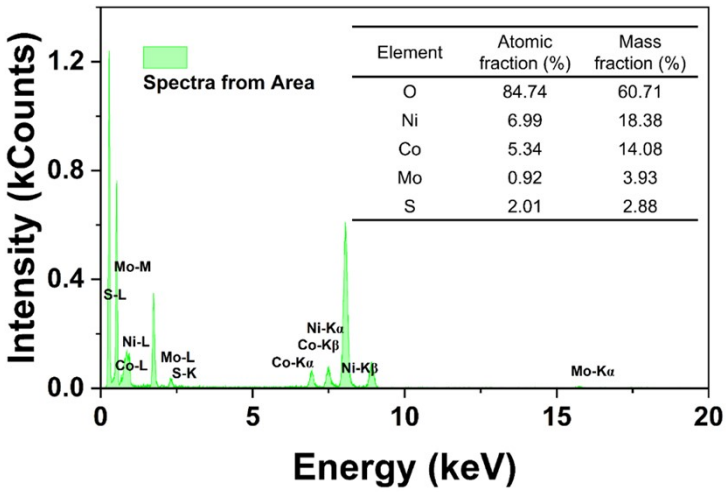

Fig. S6 Energy dispersive X-ray spectra with element contents.

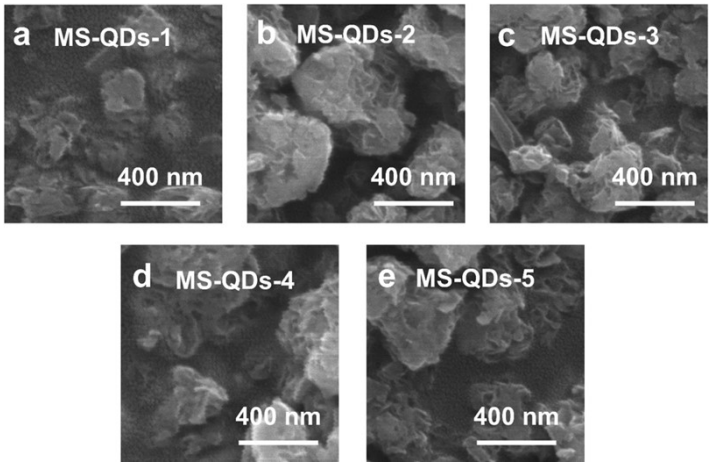

Fig. S7 SEM images of (a) MoS_2-QDs-1, (b) MoS_2-QDs-2, (c) MoS_2-QDs-3, (d) MoS_2-QDs-4, (e) MoS_2-QDs-5.

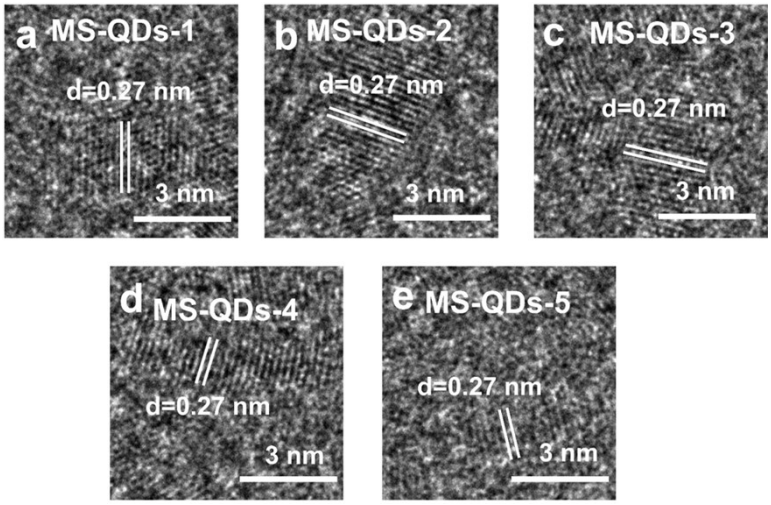

Fig. S8 HREM images of (a) MoS_2-QDs-1, (b) MoS_2-QDs-2, (c) MoS_2-QDs-3, (d) MoS_2-QDs-4, (e) MoS_2-QDs-5.

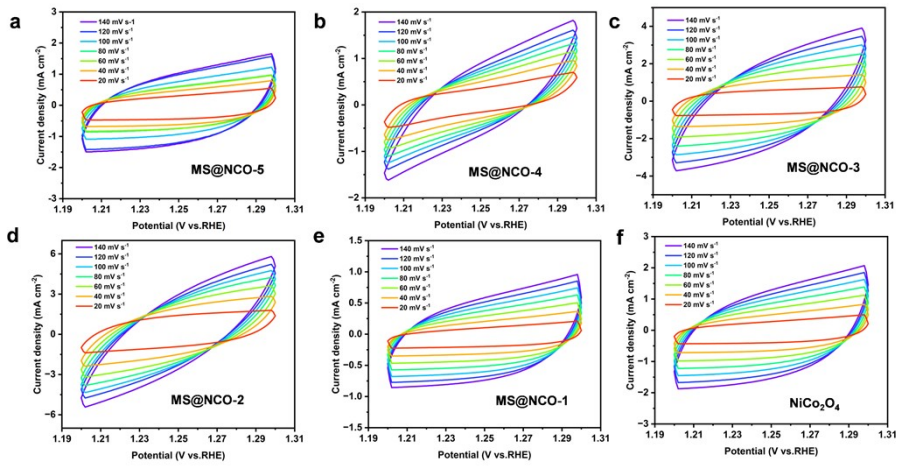

Fig. S9 CV curves of MS@NCO and $NiCo_2O_4$ at scan rates of 20–140 mV s^{-1}.

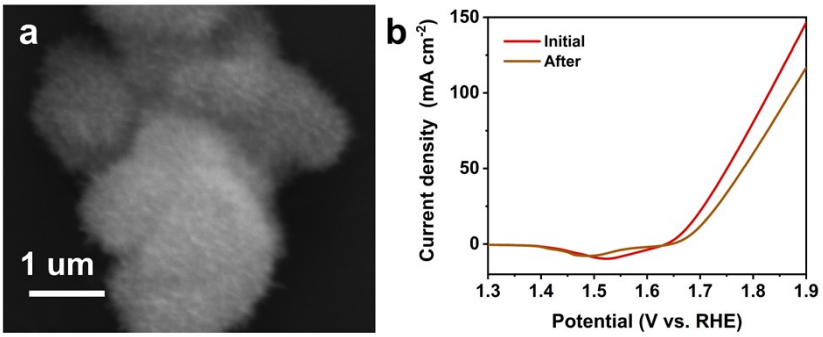

Fig. S10 (a) SEM images of MS@NCO-4 after continuous OER for 24 h, (b) LSV curves before and after stability test.

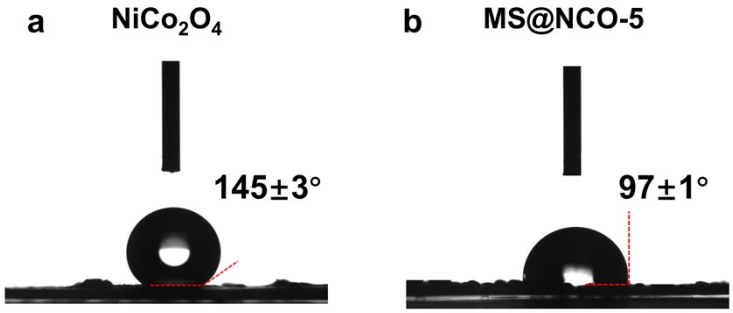

Fig. S11 Contact angle images of (a) $NiCo_2O_4$ and (b) MS@NCO-5.

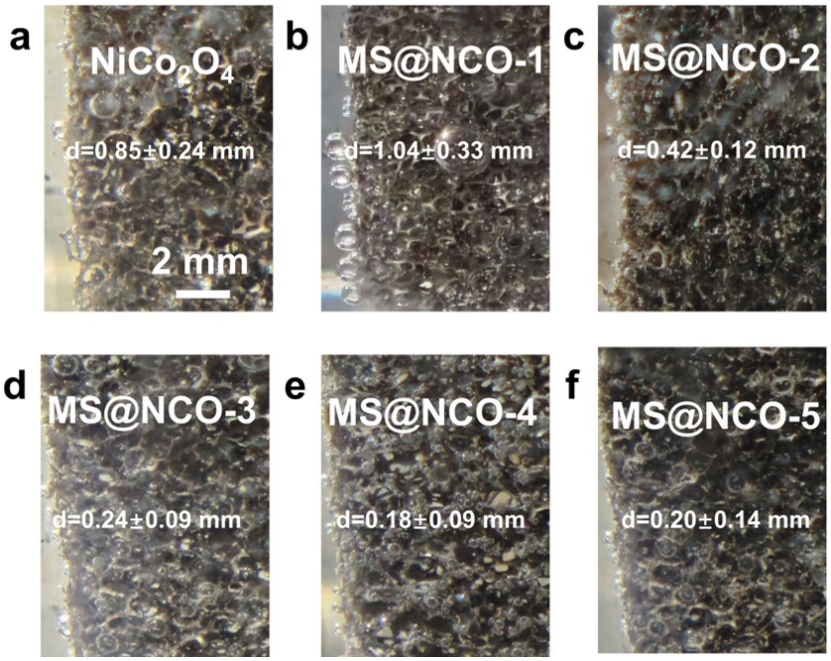

Fig.S12 Bubble evolution on the electrode surface loaded with MS@NCO and $NiCo_2O_4$ observed by optical microscope: (a) $NiCo_2O_4$; (b) MS@NCO-1; (c) MS@NCO-2; (d) MS@NCO-3; (e) MS@NCO-4; (e) MS@NCO-5

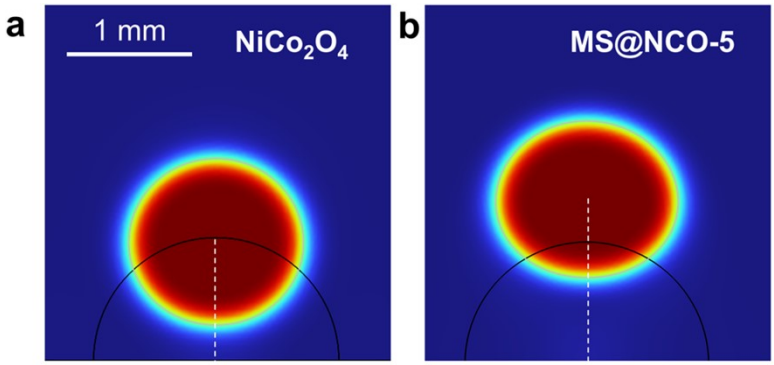

Fig. S13 Simulated oxygen bubble detachment dynamics on (a) MS@NCO and (b) MS@NCO-5 surface.

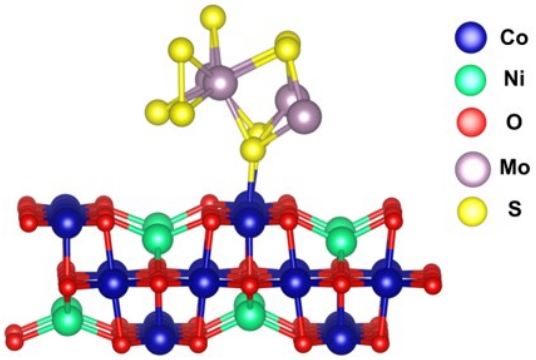

Fig. S14 Calculation model of MS@NCO.

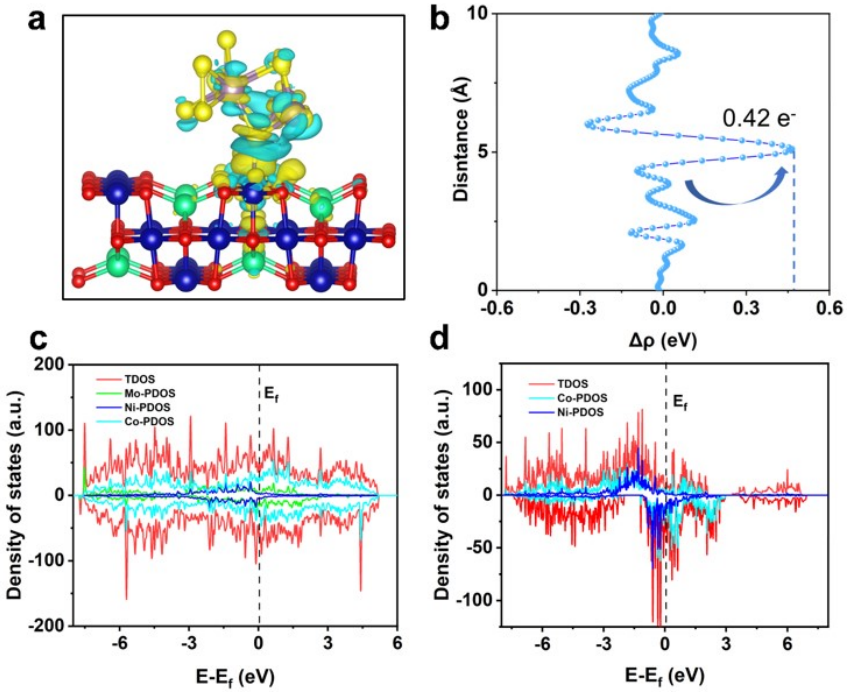

Fig. S15 (a) Differential charge density diagram. (b) Charge displacement curve of MS@NCO interface. Density of states of (c) MS@NCO and (d) $NiCo_2O_4$.

Supplementary Tables

Table S1. FTIR peak intensities of functional groups (–NH_2, –COOH) in MoS_2-QDs with varying Mo/S ratios.

Mo/S Ratio	–NH_2 (a.u.)	–COOH (a.u.)
1:1.75	0.32	0.28
1:2	0.41	0.35
1:2.25	0.53	0.47
1:2.5	0.69	0.62
1:2.75	0.65	0.55

Table S2. OER performance comparison, Tafel slope, and finite element simulation results of

MS@NCO samples.

Parameter& Sample	$NiCo_2O_4$	MS@NCO-1	MS@NCO-2	MS@NCO-3	MS@NCO-4	MS@NCO-5
η@10 mA cm^{-2} (mV)	340	325	298	285	272	278
Tafel Slope (mV dec^{-1})	122.9	100.4	96.4	84.0	76.3	79.5
R_s(Ω)	3.4	3.2	3.5	3.8	3.1	3.6
R_{ct} (Ω)	57.1	49.2	32.8	27.5	8.3	15.2
C_{dl} (mF cm^{-2})	6.3±0.5	4.9±0.3	10.4±0.8	19.8±1.7	21.7±1.5	20.5±1.2
ECSA (cm^2)	157±12	122±7	260±20	495±42	542±37	512±30

Table S3. Surface wettability and finite element simulation results of MS@NCO samples.

Parameter& Sample	$NiCo_2O_4$	MS@NCO-1	MS@NCO-2	MS@NCO-3	MS@NCO-4	MS@NCO-5
Contact Angle (°)	145	155	135	110	92	97
Detachment Distance (mm)	0.85	0.8	1.0	1.1	1.5	1.3
Detachment Time (ms)	7.5	8.9	5.9	4.3	3.5	3.8

References

1. C. Wei, S. Sun, D. Mandler, X. Wang, S. Z. Qiao and Z. J. Xu, *Chem. Soc. Rev.*, 2019, **48**, 2518-2534.

2. S. Zhu, Z. Xu, F. Chen, H. Tao, X. Tang and Y. Wang, *J. Phys. Chem. C*, 2023, **127**, 21363-21373.

3. S. Zhu, H. Tao, Y. Liu, X. Ma, K. Wang and Y. Wang, *J. Phys. Chem. B*, 2022, **126**, 10913-10921.

4. S. He, K. Wang, B. Li, H. Du, Z. Du, T. Wang, S. Li, W. Ai and W. Huang, *Adv. Mater.*, 2023, **35**, 2307017.